Molecular Content and Structure of Aqueous Organic Nanodroplets from the Vapor−Liquid Nucleation Study of the Water/*n*-Nonane/1-Alcohol Series

Ricky B. Nellas, Samuel J. Keasler, and Bin Chen*

Department of Chemistry, Louisiana State University, Baton Rouge, Louisiana 70803-1804

Received: December 4, 2007; In Final Form: January 10, 2008

Prompted by a previous finding of unusual mixing behavior for the critical clusters involved in the vapor−liquid nucleation of the ternary water/*n*-nonane/1-butanol mixture, atomistic simulations employing the AVUS-HR technique were carried out to extend such investigations to include both shorter and longer alcohols, namely, the water/*n*-nonane/$C_iH_{2i+1}OH$ mixture with $i = 2$, 4, 6, and 8. It is clear from this extensive investigation that the miscibility between water and *n*-nonane can be further improved by increasing the chain length of the alcohol (surfactant). In fact, for the water/*n*-nonane/1-octanol mixture at an intermediate gas-phase activity composition, the nucleation can proceed via fully mixed critical nuclei containing a roughly equal amount of all three components, which is in contrast to the dominantly binary-like nucleation channels observed for such mixtures involving shorter alcohols. Structural analysis revealed that these mixed nuclei take on a multilayered structural motif of the core−shell (water−alcohol) type with *n*-nonane distributed outside, forming an additional layer, more or less uniformly, compared to the one-sided deposition found for systems involving shorter alcohols. This structure provides a microscopic origin for the enhanced miscibility of water with *n*-nonane observed in the presence of 1-alcohol. These results may also have important implications for atmospheric organic aerosols.

1. Introduction

The condensation of multicomponent vapors is frequently encountered in nature and in many technological processes, from the formation of atmospheric aerosols to microemulsions, gas separations, and nanomaterials. Being a critical first step in these processes, nucleation has been the central focus for a great deal of research since the pioneering work by Volmer and Weber[1] and by Becker and Döring.[2] However, after nearly a century, molecular information on many of these atmospheric or technology-related nucleation phenomena remained elusive, until the recent emergence of novel simulation techniques that have transformed computer simulation to a complementary tool that can provide detailed molecular-level data for the nucleation process.[3−17] The AVUS-HR approach[15,16] is an example, which was developed through a combination of aggregation-volume-bias Monte Carlo (AVBMC),[18,19] umbrella sampling (US),[20] and histogram reweighting (HR).[21,22] By incorporating realistic, atomistic models in the nucleation study, this approach allows direct comparison to the experimentally measured or interpreted nucleation data and has led to a series of recent successes in simulating both single and multicomponent vapor−liquid nucleation.[13−16,23−26]

In this work, the AVUS-HR approach was applied to investigate the homogeneous vapor−liquid nucleation of the ternary water/*n*-nonane/1-alcohol series. This includes water/*n*-nonane/ethanol, water/*n*-nonane/1-butanol, water/*n*-nonane/1-hexanol, and water/*n*-nonane/1-octanol. This study was partly initiated by the experimental work of Viisanen and Strey[27] on water/*n*-nonane/1-butanol, for which a very complex nucleation behavior (evident from the onset activity plots with a concurrent appearance of multiple distinct nonideal characteristics) was reported. Some former simulations carried out by us[25,26] were found to reproduce well the experimental results for this system over the entire range of vapor-phase compositions, including both onset activities and the average content of the critical nuclei. In addition, this simulation study provided other crucial molecular details regarding the composition and structural distribution of the three components and their miscibility in the clusters. These data suggest an external separation into either water/1-butanol-enriched or *n*-nonane/1-butanol-enriched clusters even at those intermediate gas-phase compositions when the average content of the critical nuclei show equal contributions from all components involved. The fact that 1-butanol may be too short to act effectively as a surfactant for water and *n*-nonane immediately prompted this investigation of other alcohols (especially longer ones).

Apart from being of relevance to microemulsions, multiple-component mixtures that contain these three species are ideal model systems for atmospheric organic aerosols. Concern was recently raised about the composition/structure of such carbonaceous droplets due to their direct impact on cloud albedo.[28−30] In addition, these particles possess a surprisingly high organic content that cannot be fully explained by the classical homogeneous model and the aqueous solubilities of the organic compounds.[30−33] In these organic aerosols, long chain amphiphiles (e.g., polyacids) were involved as an important component, which are well-known to cause a nonuniform structural/composition arrangement when mixing with either more polar species such as water or the more nonpolar hydrocarbon components. A core−shell (water−surfactant) structure has been proposed as a motif for explaining the high organic content for these atmospheric aerosols.[31−33] This speculation has been directly confirmed by small angle neutron scattering experiments on nanodroplets formed by water and 1-butanol[34] and also by simulations,[23−26,35] e.g., for binary water/

* Corresponding author. E-mail: binchen@lsu.edu.

10.1021/jp711452r CCC: $40.75 © 2008 American Chemical Society
Published on Web 02/27/2008

ethanol and ternary water/*n*-nonane/1-butanol clusters. Here it will be shown that the core−shell structure formed by longer alcohols (a better mimic of polyacids and other surfactant molecules) can further attract less polar organic materials (such as purely nonpolar alkanes) onto the cluster surface, which would not only lead to an enriched carbon content but also have some new implications for the properties of those atmospheric droplets.

Presented in the next section are a brief description of the AVUS-HR nucleation simulation approach, the molecular force fields, and simulation conditions used in this investigation. The simulation results are presented and discussed in section 3, and section 4 provides concluding remarks.

2. Simulation Details

Being an activated event, nucleation can be characterized by a free energy (NFE) profile expressed as a function of order parameters, e.g., cluster size for single-component systems and also composition for multicomponent vapor−liquid nucleation (or numbers of molecules of each component contained by the cluster, i.e., $\{n_i\}$). Constructing this NFE landscape, $\Delta G(\{n_i\})$, or equivalently the cluster probability, $P(\{n_i\}) = \exp[-\Delta G(\{n_i\})/k_BT]$, becomes the major task for simulation. The simulation methodology employed here (AVUS-HR)[15,16] was developed for this purpose and has led to our recent success in simulating a series of vapor−liquid nucleation events. Its efficiency in sampling rare events such as nucleation arises from the incorporation of several advanced simulation methods, including aggregation-volume-bias Monte Carlo (AVBMC),[18,19] self-adaptive umbrella sampling (US),[20] and histogram reweighting (HR).[21,22] While the former two are specifically used to overcome the major sampling difficulties encountered in nucleation events, such as the inherent microheterogeneity of the phase space and the low occurrence probabilities for clusters near the critical size, the latter is introduced to interpret the probability (or free energy) information for neighboring thermodynamic states *without additional simulations*. In particular, AVBMC is a special technique developed by us (originally directed toward strongly associating fluids)[18,19] to circumvent the long time scales required for particles to diffuse together in the gas phase and for the reverse particle evaporation from the cluster phase, by employing direct swap moves between monomer and cluster phases. The incorporation of the configurational-bias Monte Carlo (CBMC) scheme[36−38] further improves the acceptance rates for the AVBMC swaps and most importantly allows the extension of this method to molecules with articulated structures, modeled by realistic, atom-based force fields for direct comparisons with the experiments.

The simulations reported here were all carried out using the grand-canonical version of the nucleation algorithm.[13,14] The NFE data were evaluated for all clusters of interest (i.e., up to a size slightly larger than the critical clusters) at only one set of gas-phase activities $\{a_1^O, a_2^O, a_3^O\}$, which was directly specified as part of the simulation conditions. Interpretations at other conditions $\{a_1^N, a_2^N, a_3^N\}$ were then made using the following equation,[26]

$$\Delta G_{a_1^N,a_2^N,a_3^N}(n_1,n_2,n_3) = \Delta G_{a_1^O,a_2^O,a_3^O}(n_1,n_2,n_3) - \sum_{i=1}^{3} n_i \times k_BT \ln(a_i^N/a_i^O) \quad (1)$$

Note that the zero reference point for the NFE data reported here was set to a concentration of 1 droplet/Å^3 so that the NFE values can be directly converted to absolute concentrations expressed in this unit. This interpretation allows us to map all the possible combinations of gas-phase activities that would yield similar barrier heights (or nucleation rates) for the construction of the onset activity plots.

Following previous work,[16,26] a constant combined nucleation barrier height of 50.64 k_BT (corresponding to a critical cluster concentration of 10^{-22} droplets/Å^3 or 100 droplets/cm^3) was used to determine the onset activities. For the ternary systems investigated here, in the calculation of this combined barrier, the cluster probability information, $P(n_1,n_2,n_3)$, was projected onto a single coordinate, the combined size of the cluster n ($=n_1 + n_2 + n_3$). Specifically, for a cluster with a total size of n, its overall concentration $P^{tot}(n)$ is obtained by

$$P^{tot}(n) = \sum_{n_1=0}^{n} \sum_{n_2=0}^{n-n_1} P(n_1,n_2,n-n_1-n_2) \quad (2)$$

Then $P^{tot}(n)$ can be converted back to the combined NFE for this given cluster size, $\Delta G^{tot}(n) = -k_BT \ln P^{tot}(n)$. This combined nucleation barrier allows us to take into account the contributions from all possible pathways (critical nuclei) present on the NFE map, which is important for multicomponent systems. With this one-dimensional free energy plot, the determination of the barrier height and critical cluster size is straightforward (similar to single-component nucleation).

While water was modeled by TIP4P,[39] the TraPPE-UA[40,41] force field was used for both *n*-nonane and 1-alcohol. As chain molecules were involved in these simulations, we employed an energy-based Stillinger-type cluster criterion;[42] that is, a cluster is defined as a group of molecules in which every molecule has at least one neighbor in the group with an interaction energy less than U_{cl}. Following our previous ternary nucleation work on water/*n*-nonane/1-butanol,[26] U_{cl} is set to -260 k_B for all pairs of like or unlike molecules except for the water/*n*-nonane pair and the *n*-nonane/1-alcohol pair for which U_{cl} is set to -30 and -120 k_B, respectively. It has been shown that the nucleation free energy results are relatively insensitive to the choice of the cluster criterion.[14,15] All simulations were carried out at $T = 230$ K, which is around the condition range accessible by the nucleation pulse chamber experiments for such systems (but only water/*n*-nonane/1-butanol has been studied experimentally).[27] Each cluster of a specific size and composition was visited at least 10^5 times and on average more than 10^6 times.

3. Simulation Results and Discussions

A. Plots of the Onset Activities. Plotted in Figure 1 are the various combinations of onset activities, $\{a_i\}$, with $i = 1$, 2, and 3, denoting water, *n*-nonane, and 1-alcohol, respectively, obtained for a constant combined barrier height of 50.64 k_BT (only the data for water/*n*-nonane/1-hexanol were shown and the other systems exhibit similar features). Because only two of the three a_i's are independent, the onset activity data form a surface in a three-dimensional $a_1-a_2-a_3$ space (represented by a mesh-network in Figure 1). These a_i's have been normalized by the activities of the corresponding neat component. Thus, the onset activity surface crosses each of the three axes with a unit value, where unary onset nucleation of each of the three components occurs.

Shown in Figure 2 are a discretized group of onset activity curves obtained at the conditions used by Viisanen and Strey[27] in their pulse chamber experiment for the water/*n*-nonane/1-butanol system. These conditions can be classified on the basis of the value of the normalized activity fraction of *n*-nonane,

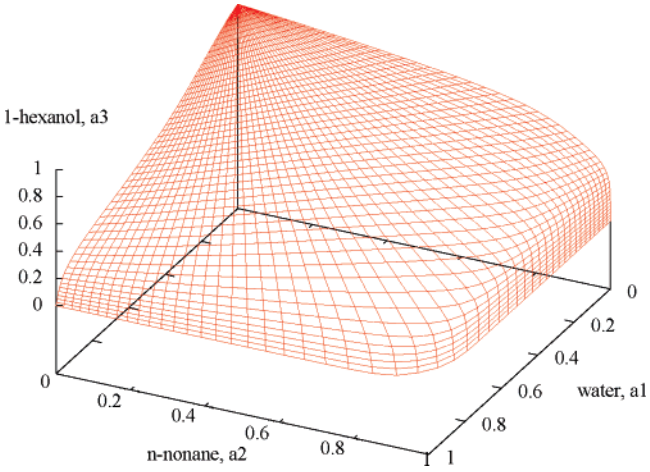

Figure 1. Entire onset activity surface obtained for the water/*n*-nonane/1-hexanol system from the simulation at a constant combined barrier height of 50.64 k_BT.

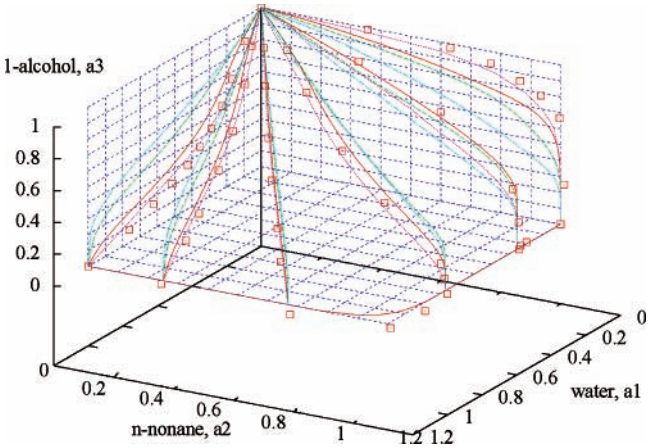

Figure 2. Onset activity curves obtained at a discretized set of a_2' varying from 0 to 1 at intervals of 0.2 for water/*n*-nonane/ethanol (magenta), water/*n*-nonane/1-butanol (red), water/*n*-nonane/1-hexanol (green), and water/*n*-nonane/1-octanol (cyan). The experimental data[27] obtained for water/*n*-nonane/1-butanol at 240 K are also included as red squares.

a_2', defined as $a_2/(a_1 + a_2)$, which changes from 0 to 1 in intervals of 0.2. For comparison, their experimental data were also included in Figure 2. As is evident from this figure, the simulation data capture very well the several distinct types of nonideal characteristics exhibited by the experimental onset activity results for this ternary system at the different vapor-phase composition conditions. Also this rather diverse set of features seem to be common for the ternary water/*n*-nonane/1-alcohol series (at least up to 1-octanol). For example, at low a_2' conditions, a sign of mutual nucleation enhancement is prominent, especially for shorter alcohols, with the combined activity lower than the unit value expected for an ideal mixture (similar to water/1-alcohol). On the contrary, when a_2' is high, the onset activity plots show a dominant reluctant conucleation feature, with the combined activity higher than for an ideal mixture (similar to binary *n*-nonane/1-alcohol). On the other hand, both features were found to be present in the onset activity plot obtained at intermediate a_2' conditions.

B. Core−Shell Structures Formed by the Water/1-Alcohol Clusters and Comparison to the Experimental Data for This Binary Series. Note that experimental data for this ternary series are only available for water/*n*-nonane/1-butanol, whereas extensive nucleation rate measurements have been carried out by Strey and co-workers for binary *n*-nonane/1-alcohol[43] and water/1-alcohol systems (up to 1-hexanol).[44,45] The ternary nucleation simulations reported here allow a convenient examination of these two groups of binary systems (by setting a_2' to either one or zero) to compare with the experimental data. For the former series, this comparison has already been done by us previously[16] and thus will not be repeated here. Important results are (i) the simulation data reproduced well the nonideal reluctant conucleation characteristics reported previously from the experiment[43] on the *n*-nonane/1-alcohol series and (ii) when this series moves away from the miscibility gap, the nucleation mechanism evolves from a two-pathway type for *n*-nonane/methanol to a single-pathway mechanism for *n*-nonane mixed with longer alcohols, and passes through a multiple-pathway-like mechanism for those intermediate cases involving medium-length alcohols such as ethanol. This microscopic miscibility information matches well with the macroscopic miscibility data for these two species. For example, methanol and *n*-nonane are known to have a miscibility gap, which vanishes quickly with increasing alcohol chain length.

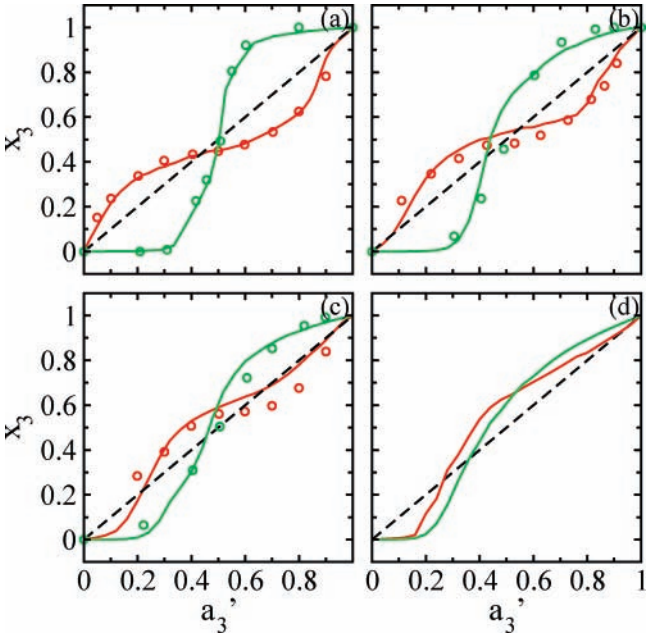

Figure 3. Average mole fraction of 1-alcohol in the critical nuclei as a function of its activity fraction obtained for binary (a) water/ethanol, (b) water/1-butanol, (c) water/1-hexanol, and (d) water/1-octanol. For comparison, the data obtained for the binary *n*-nonane/1-alcohol series are also shown (in green). The symbols and lines denote the experimental data[43,45] and simulation results, respectively. The dashed straight line corresponds to the ideal case.

Similar to the *n*-nonane/1-alcohol series, the macroscopic miscibility between water and 1-alcohol also exhibits a chain-length dependence but in this case decreases with the number of carbon atoms in the alcohol. For example, 1-butanol is the shortest 1-alcohol that already displays a miscibility gap with water. Although the maximum water solubility in 1-butanol (or longer alcohols) is about 0.5 (or lower) in terms of mole fraction, the alcohol solubility in water drops rapidly with increasing chain length and is below 0.02 for all except the fully miscible alcohols.[45] In contrast, the molecular content of the critical nuclei inferred from the experimental nucleation rate[45] through the nucleation theorem[46,47] indicated that the average composition could range continuously from pure water to pure alcohol irrespective of the alcohol chain length (see Figure 3). The results from our simulation are not much different. In fact, the two sets of results (calculated versus experimental[43−35]), plotted as a function of the normalized activity fraction of 1-alcohol,

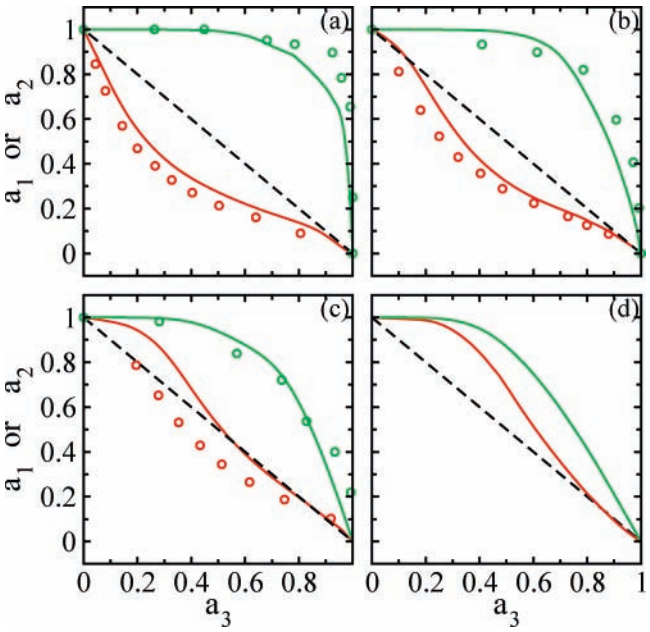

Figure 4. Plots of the reduced onset activities for the binary water/1-alcohol and *n*-nonane/1-alcohol series. Symbols and panels are the same as Figure 3.

a_3', defined as $a_3/(a_1 + a_2 + a_3)$, follow each other closely. For ideal mixtures, it is expected that these data will fall onto a straight-line linked by the two end points that correspond to the unary nucleation of either water or 1-alcohol (see the dashed line included in Figure 3). Clearly, both the simulation and experimental data show a certain degree of enrichment of 1-alcohol at low 1-alcohol activity or enrichment of water at low water activity, especially for shorter alcohols. This behavior is just the opposite of that found for the *n*-nonane/1-alcohol systems, for which the results were shown in Figure 3 as well. Also distinct from *n*-nonane/1-alcohol are the mutual nucleation enhancement characteristics exhibited by the onset activity plots (see Figure 4), with a concave-down curvature versus concave-up (signaling reluctant conucleation) for *n*-nonane/1-alcohol. This feature gradually diminishes toward longer alcohols. Actually, for both 1-hexanol and 1-octanol, the simulation data show the presence of a region (at low alcohol activity conditions) with the combined activities higher than the unit value expected for an ideal mixture, resembling to some extent the reluctant conucleation feature of the *n*-nonane/1-alcohol system, which is also consistent with the depletion of the alcohol over that range of conditions (see Figure 3).

It should be mentioned that for mixtures approaching or already showing macroscopic miscibility, the average composition alone cannot completely rule out the possibility of external phase separation for these cluster systems or the coexistence of multiple critical nuclei, each having a unique composition that can be significantly different from the average composition.[16,23−26,48−52] To further examine the miscibility information, the nucleation free energy contours detailing the probabilities of observing clusters of all compositions were displayed in Figure 5 (for a condition when the average composition of the critical nuclei indicates equal amounts of both components). Only the data obtained for the water/1-hexanol mixture were shown as they are quite representative of the rest of the systems (including the fully miscible water/ethanol). Despite the fact that water/1-hexanol has a macroscopic miscibility gap (and the models used here have been shown to be able to predict such bulk-phase separation behavior for the water/1-alcohol mixture),[53,54] only one major type of critical nuclei (and correspondingly a single nucleation pathway) can be identified from the NFE map shown in Figure 5, with the most probable composition close to 15 molecules of each type. This provides direct support for the notion that small clusters can have different miscibility behavior from the bulk systems.

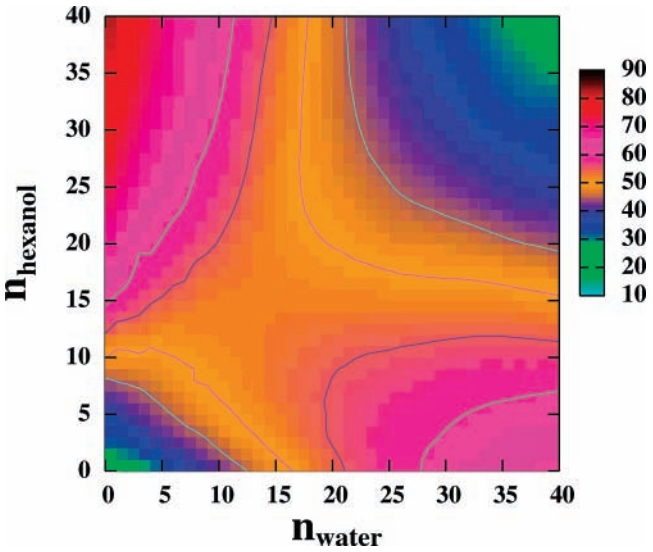

Figure 5. Contour plot of the two-dimensional NFE (in units of k_BT) as a function of the number of water and 1-hexanol molecules calculated from the simulation at $a_1 = 0.68$ and $a_3 = 0.40$. The contour levels with NFE values of 45, 50, 55, and 60 k_BT were depicted as lines for a clear view of the NFE profiles near the saddle point.

It was speculated by Strey and co-workers[45] that the enrichment of 1-alcohol at the cluster surface, i.e., in a structural motif of the core−shell (water−alcohol) type, may be the source of the deviation for these microscopic miscibility data compared to their bulk counterparts. This structure has been confirmed previously for systems involving shorter alcohols (e.g., ethanol and 1-butanol) by molecular dynamics[35] and Monte Carlo[23−26] simulations and lately by experiments[34] as well on clusters that are several orders of magnitude larger than the critical clusters found here.[34] Here clusters containing longer alcohols also adopt a dominantly core−shell motif (see Figure 6). This result is expected considering that all alcohol molecules are capable of developing Langmuir monolayers at the water surface. In fact, through the formation of such monolayer structures, both water and alcohol can benefit from the additional hydrogen bonds formed between the excess free hydrogens of surface water and the excess hydrogen bond acceptor sites of alcohol.[23,53] For example, for single-component clusters of size 40, the average number of hydrogen bonds is 3.27 per water (or 2.00 per 1-hexanol) molecule, whereas this number increases to 3.80 per water (or 2.18 per 1-hexanol) for mixed clusters, using the criteria: $r_{OH} < 2.5$Å and $-1 < \cos\theta_{OH\cdots O} < -0.4$.[23] This surface monolayer is also the reason for the mutual nucleation enhancement observed especially for shorter alcohols as it greatly lowers the surface tension and correspondingly the surface free energy of the cluster formation.[53] However, for these cluster systems the formation of the curved monolayer structures comes at a price of losing some of the attractive interactions between the alcohol alkyl tails. This factor becomes more important with increasing alcohol chain length and is part of the reason for the gradual disappearance of the mutual nucleation enhancement feature (see Figure 4c,d) and for the depletion of the alcohol at low alcohol activity fraction as the chain length increases (see Figure 3c,d). In particular, depositing an individual alcohol molecule on the water surface would be unfavorable due to the absence of alkyl tail interactions. Correspondingly,

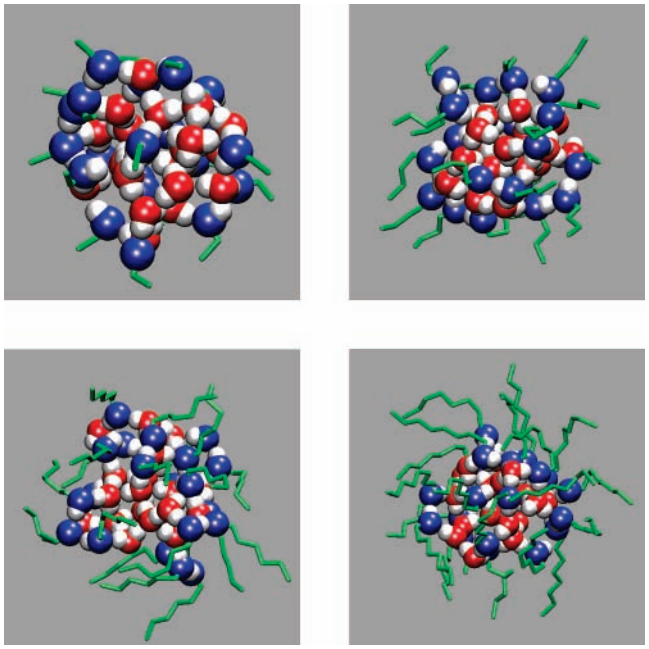

Figure 6. Representative snapshots of binary water/1-alcohol clusters (consisting of 20 molecules of each component) obtained from the four systems using alcohols of different chain lengths. Color notation: water oxygen (red); 1-alcohol oxygen (blue); hydrogen (white); and alkyl tails (green stick).

the alcohol monolayer is formed through a more collective process (triggered also by a further increase of the alcohol activity for longer chains), which explains the sudden jump in the 1-alcohol content of clusters at an a_3' value of around 0.2 (see Figure 3c,d).

C. Enhanced Miscibility between Water and *n*-Nonane Due to the Presence of Alcohols via the Core−Shell Motif. Being an amphiphile and sharing components that are alike to both polar water and nonpolar alkanes, alcohols are expected to improve the miscibility between these two species. The core−shell motif formed between water and 1-alcohol shown in Figure 6 has already provided some structural hints for this enhanced miscibility. In particular, the nonpolar surface (covered by the alkyl tails of the alcohols) becomes more attractive for the adsorption of the purely nonpolar *n*-nonane than the original bare water surface. Indeed, mixed clusters containing equal amounts of these three components show a dominantly "onion"-like[25] core−shell motif with *n*-nonane deposited outside forming an additional layer (see Figure 7). This enhanced miscibility mechanism is also evident when comparing these structures to those formed solely between water and *n*-nonane (see Figure 7a), where these two incompatible components display a consistent preference to segregate from each other forming two individual droplets. This type of phase separation remains prominent even in the presence of short alcohols (such as ethanol and 1-butanol, see Figure 7b−d) or a limited number of longer 1-alcohol molecules (see Figure 7e,g). In the latter case, the clusters are shaped more like a dumbbell and the addition of a few alcohol molecules simply introduces a surfactant handle to link the water and oil droplets together.[25] However, with the addition of more alcohol molecules into the clusters, the dumbbell structure quickly evolves into the onion due to the tendency for the alcohols to be distributed around the water surface to form the core−shell motif. For longer alcohols, this structural transformation also induces a more uniform dispersion of *n*-nonane molecules around this core−shell structure (see Figure 7f,h), forming an additional onion-like layer on the outside, in contrast to the one-sided deposition of *n*-nonane (which remained as an oil droplet) found for clusters containing shorter alcohols (see Figure 7b−d). Clearly, for the latter cases *n*-nonane molecules still prefer to interact with themselves rather than with the short nonpolar tails of either ethanol or 1-butanol. On the contrary, longer alcohols appear to act more effectively as an amphiphile, bringing water and *n*-nonane together to form a more symmetrical spherical structure. Thus, from the structural evolution depicted in Figure 7 it is tempting to suggest that the miscibility between water and *n*-nonane can be further improved by increasing the alcohol chain length.

Evidence of the enhanced miscibility between water and *n*-nonane in the presence of the longer alcohols comes from the composition analysis. It has been shown that the ternary nucleation of water/*n*-nonane/1-butanol behaves pretty much like a binary water/1-butanol system when a_2' is low, with *n*-nonane almost completely excluded from the critical clusters.[26] This was reflected by the average composition plots (see Figure 8), where the mole fraction of *n*-nonane was found to be very close to zero by both the simulation and the experiment[27] but the contributions of the other two components to the critical clusters stay nearly the same up to an a_2' value of 0.4 for the ternary water/*n*-nonane/1-butanol mixture. Similar results were also obtained for water/*n*-nonane/ethanol (and thus they were not included in this figure). In contrast, for longer alcohols continuous changes were observed in the average content of the critical nuclei over the same range of a_2'. In particular, with an increase of a_2' from 0 to 0.4, *n*-nonane emerges as a component that is no longer negligible in the nucleation process. In addition, its contribution to the critical nuclei improves steadily with the alcohol chain length (and could be even more significant if longer alcohols were used). Such an enhanced *n*-nonane content is also accompanied by a slightly higher 1-butanol mole fraction and a lower water contribution to the critical cluster.

From the composition results obtained at low a_2' conditions, one may speculate that the miscibility between water and *n*-nonane would continue to improve with a further increase of a_2'. However, an immediate complication is the appearance of another group of clusters, dominantly composed of *n*-nonane, which are already observed at $a_2' = 0.5$. In particular, for all cases shown in Figure 8 the composition plots revealed a revolutionary change at $a_2' = 0.5$ with *n*-nonane starting to replace water as a major component in the critical nuclei (especially toward low a_3 conditions), whereas at the transition point roughly equal amounts of *n*-nonane and water could be found in the critical nuclei even when 1-alcohol is absent. As mentioned previously,[23,24] a mole fraction close to 0.5 for both water and *n*-nonane observed at those conditions should not be used as a sign of miscibility between these two components. Rather, it is due to the formation of two major critical nuclei, one water-enriched and the other *n*-nonane-enriched. Intuitively, one can also rule out the possibility of forming fully mixed critical nuclei given that the mole fraction of *n*-nonane even decreases with the addition of alcohol to the critical nuclei (see Figure 8). This decrease is initially compensated by the increase of both water and 1-alcohol content. Eventually, the mole fraction of water goes down after reaching a maximum at a certain a_3 value. This feature stays qualitatively the same for higher a_2' conditions in the different systems examined here except that the water mole fraction decreases with increasing a_2' or with alcohol chain length. Therefore, it is generally expected that both water- and *n*-nonane-enriched critical clusters could coexist with each other at those conditions. As a result,

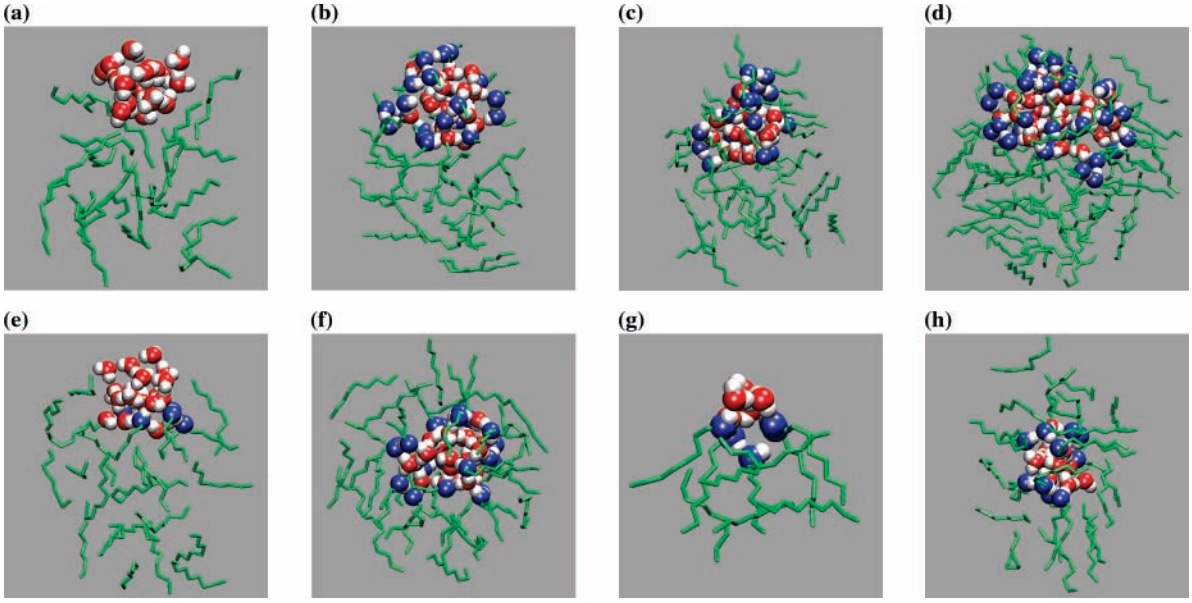

Figure 7. Representative snapshots for mixed clusters consisting of (a) 20 water and 20 *n*-nonane; (b) 20 water, 20 *n*-nonane, and 20 ethanol; (c) 20 water, 20 *n*-nonane, and 20 1-butanol; (d) 40 water, 40 *n*-nonane, and 40 1-butanol; (e) 20 water, 20 *n*-nonane, and 5 1-hexanol; (f) 20 water, 20 *n*-nonane, and 20 1-hexanol; (g) 5 water, 5 *n*-nonane, and 5 1-octanol; and (h) 12 water, 12 *n*-nonane, and 12 1-octanol. Color notation as in Figure 6.

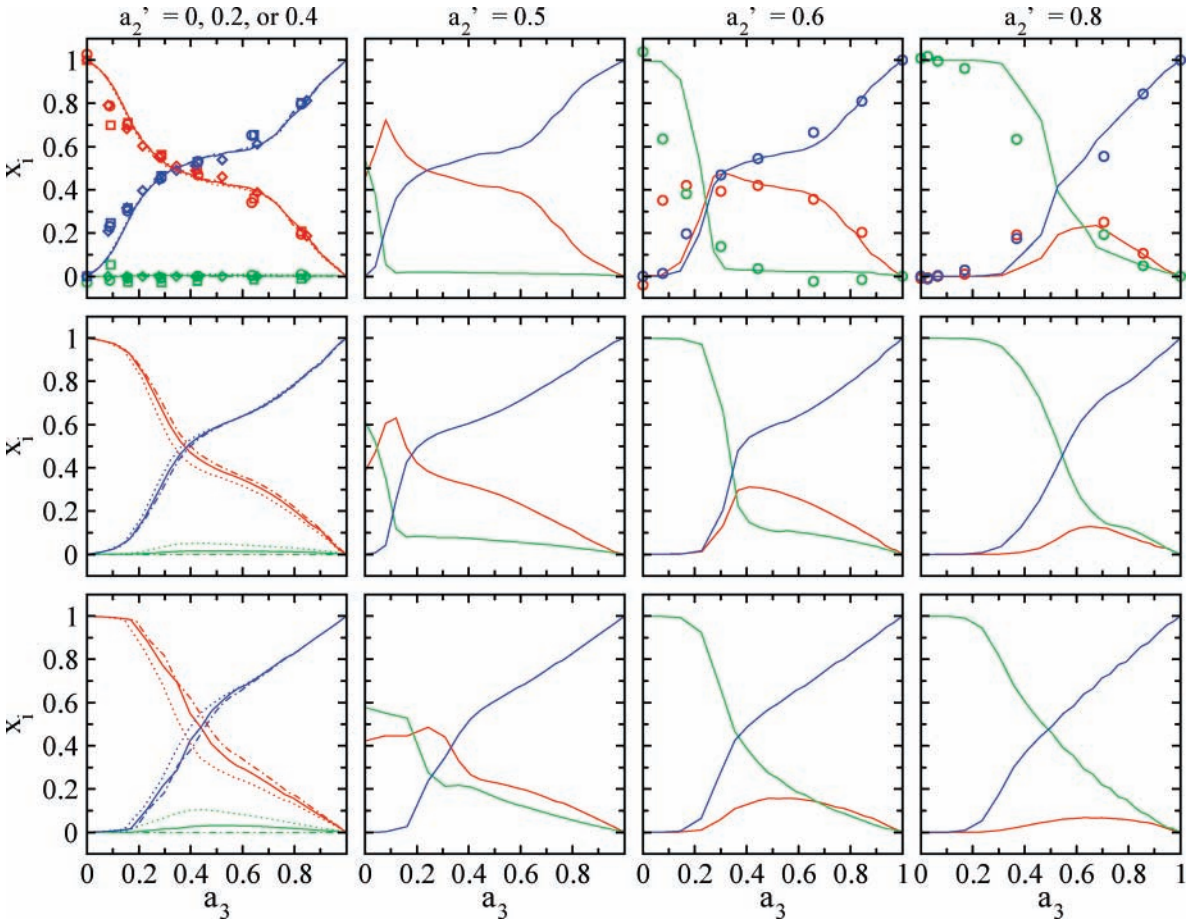

Figure 8. Average mole fraction of water (red), *n*-nonane (green), and 1-alcohol (blue) as a function of the normalized activity of 1-alcohol obtained at an a_2' value of 0 (diamonds and dashed-dotted lines), 0.2 (circles and solids lines), 0.4 (squares and dotted lines), and other a_2's as specified at the top of each column. The top, middle, and bottom panels represent the results obtained for the ternary systems involving 1-butanol, 1-hexanol, and 1-octanol, respectively. The experimental data[27] obtained for water/*n*-nonane/1-butanol are also included as symbols.

the composition data plotted in Figure 8 may not be directly reflective of the miscibility for these cluster systems.

For those conditions where the average composition plots show the largest miscibility between the three components, the NFE contour maps were taken out specifically around the critical cluster size for a detailed view of the miscibility information between these three components. As shown in Figure 9, for conditions with a_2' below 0.4, only water-enriched critical

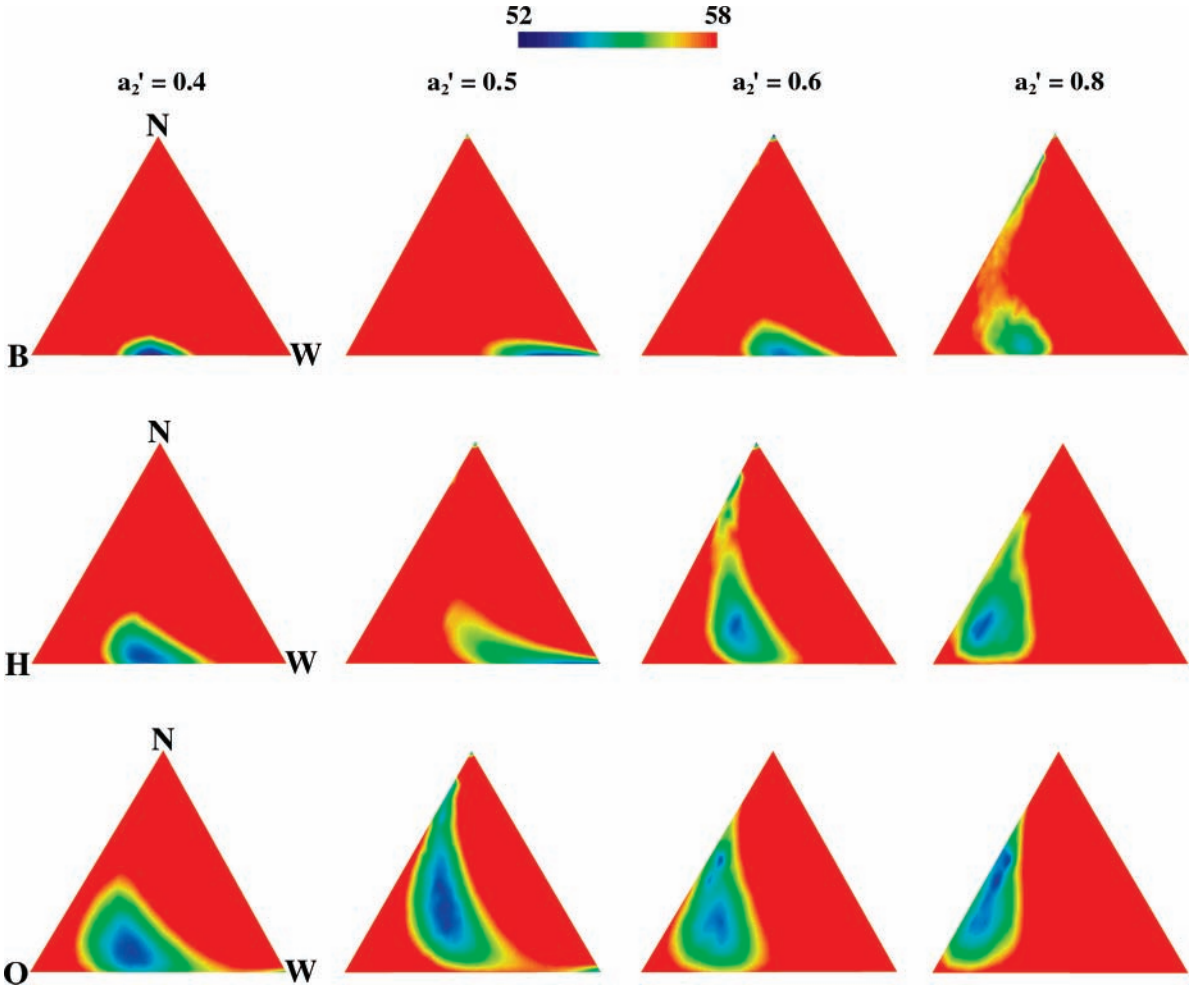

Figure 9. NFEs (in units of k_BT) as a function of cluster composition. The top four panels represent the results obtained for water/*n*-nonane/1-butanol (W/N/B), from left to right, at (a) $a_1 = 0.41$, $a_2 = 0.27$, $a_3 = 0.40$, and a cluster size of 42; (b) $a_1 = 0.87$, $a_2 = 0.87$, $a_3 = 0.12$, and a cluster size of 33; (c) $a_1 = 0.61$, $a_2 = 0.91$, $a_3 = 0.25$, and a cluster size of 30; and (d) $a_1 = 0.19$, $a_2 = 0.78$, $a_3 = 0.62$, and a cluster size of 42. The middle four panels represent the results obtained for water/*n*-nonane/1-hexanol (W/N/H), from left to right, at (a) $a_1 = 0.62$, $a_2 = 0.42$, $a_3 = 0.40$, and a cluster size of 27; (b) $a_1 = 0.90$, $a_2 = 0.90$, $a_3 = 0.22$, and a cluster size of 30; (c) $a_1 = 0.60$, $a_2 = 0.90$, $a_3 = 0.36$, and a cluster size of 24; and (d) $a_1 = 0.17$, $a_2 = 0.68$, $a_3 = 0.65$, and a cluster size of 27. The bottom four panels represent the results obtained for water/*n*-nonane/1-octanol (W/N/O), from left to right, at (a) $a_1 = 0.74$, $a_2 = 0.49$, $a_3 = 0.40$, and a cluster size of 21; (b) $a_1 = 0.88$, $a_2 = 0.88$, $a_3 = 0.26$, and a cluster size of 27; (c) $a_1 = 0.42$, $a_2 = 0.63$, $a_3 = 0.48$, and a cluster size of 21; and (d) $a_1 = 0.15$, $a_2 = 0.58$, $a_3 = 0.60$, and a cluster size of 21.

clusters are present on these maps with the most probable compositions (colored in blue) centered around those average values shown in Figure 8. Thus, consistent with the average composition data, the increase of either the alcohol chain length or a_2' leads to a steady shift of this blue domain from the water/1-alcohol binary line to the inner region of this triangular "nanophase diagram". Further increasing a_2' leads to the appearance of *n*-nonane-enriched critical clusters coexisting with water-enriched critical clusters (in accord with our expectation). Such external phase separation is already quite pronounced at $a_2' = 0.5$ with these diagrams displaying at least two separate blue domains (to represent these two types of most probable critical clusters). For water/*n*-nonane/1-butanol, the coexistence of these two cluster phases is also revealed at higher a_2' and appears to be a universal feature for those conditions as long as the average content of the critical nuclei suggests the substantial presence of all components. On the contrary, when the longer alcohols are used as the surfactant, a merging of these multiple phases into a fully mixed one, which still contains appreciable amount of all components, could occur at higher a_2' conditions (see the three diagrams located at the lower-right corner of Figure 9, each displaying essentially one major blue domain, although it is widely spread out and located close to the *n*-nonane/1-alcohol line). This provides direct support for the further improved miscibility between water and *n*-nonane in the presence of the longer alcohols. But among all the maps displayed in Figure 9, the most striking evidence for such enhanced miscibility is actually provided by the water/*n*-nonane/1-octanol system at an intermediate vapor-phase composition condition (i.e., at an a_2' value of 0.5), in which a blue domain emerged right around the center of the triangular "nanophase diagram". A more surprising feature of this NFE map is the coexistence of these fully mixed critical clusters with the other two major critical nuclei, enriched by either water or *n*-nonane (see the other two blue regions located at either the water or the *n*-nonane end). This is in sharp contrast to the rest, which show at most two major cluster phases in coexistence, with each phase typically enriched by one or two but rarely all three components, and thus implying an even more complex nucleation mechanism than previously described for multiple-component nucleation of this type.

To resolve the mechanistic details for this particular case, the NFEs were analyzed for both pre- and post-critical clusters and these results are shown in Figure 10. It becomes apparent from these additional NFE maps that nucleation for this mixture originally proceeds through externally phase-separated clusters,

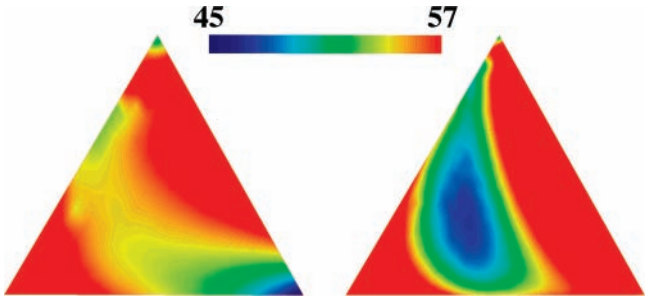

Figure 10. NFEs (in units of k_BT) as function of cluster composition obtained for the water/*n*-nonane/1-octanol system at $a_1 = 0.88$, $a_2 = 0.88$, and $a_3 = 0.26$ for pre-critical clusters consisting of 15 molecules (left) or post-critical clusters of 39 molecules (right).

especially those enriched almost exclusively by water (see the left NFE map obtained at a cluster size of 15 with the blue region located toward the water end in Figure 10). Although this map also indicates the presence of *n*-nonane-enriched clusters, their population is expected to be much smaller than the water-enriched ones given the exponential dependence of the population on the NFE value. The probability to observe fully mixed clusters at this cluster size is even lower as the center region of this diagram shows significantly higher NFE values than either the water or the *n*-nonane side. However, with increasing cluster size, the relative thermodynamic stability of these fully mixed clusters versus those phase-separated ones improves continuously. As already shown by the NFE map in Figure 9, around the critical cluster size the occurrence frequency for these mixed clusters becomes roughly comparable to the phase-separated ones at this condition. Further increasing the cluster size favors these fully mixed clusters even more and eventually makes them the dominant type of clusters on the nucleation landscape (see the right NFE map obtained at a post-critical cluster size of 39 in Figure 10).

It should be noted that such a steadily improved stability for the fully mixed clusters with increasing size is expected from the structural evolution depicted in Figure 7 and the fact that the number of alcohol molecules contained by these clusters is directly proportional to the cluster size. As shown by Figure 7g, with the number of alcohol molecules too low to cover the water droplet, small fully mixed clusters (with a size of 15 or below) adopt a dumbbell motif. Although this structure allows the alcohol molecules to interact fully with both water and *n*-nonane, the exposure of the water surface to the outside is extremely unfavorable for the overall stability (due to the large surface tension and surface free energy penalties). Clearly the core−shell structure (as shown in Figure 7h) is better in this regard (and thus more stable) but is only a viable form for larger clusters when enough alcohol molecules are present. Correspondingly, with increasing cluster size, fully mixed clusters evolve from a dumbbell-like structure to a dominantly core−shell motif. The significantly improved thermodynamic stability from such a structural transition is therefore directly in coherence with the dramatic evolution of those "nanophase diagrams" shown in Figure 10.

Further support for this structural transformation comes from the density profiles (see Figure 11). Inspired by the dumbbell motif, these probability density profiles were analyzed using the following procedure. First, the center of mass (COM) was calculated separately for the two droplets formed by either water or *n*-nonane molecules. Then an axis (denoted as the "z"-axis in Figure 11) was created by linking these two COMs, with its origin fixed at the COM of the water droplet and its positive side pointing to the COM of the *n*-nonane droplet. Finally the probability density of each atom type was computed and normalized along this "z"-axis. For each cluster of a given size and composition, about 100 independent configurations were used to obtain the data shown in Figure 11. As evident for small clusters the density profiles display the type of separation expected for a dumbbell motif, with the peak moving from left to right for the water oxygen, 1-octanol oxygen, 1-octanol carbon, and *n*-nonane carbon (see Figure 11a). In addition, the left-side of the water droplet is almost fully exposed to the outside. Only occasionally would one or two *n*-nonane molecules dangle away from the *n*-nonane droplet to interact with the water molecules (see Figure 7a,e), which causes the long tailing of the *n*-nonane carbon density profile into the negative side of the *z*-axis. Although these density distributions were found to be highly unsymmetrical with respect to the COM of the water droplet at small cluster sizes, they were more or less centered for larger clusters containing 30 molecules or more (see Figure 11b), which is a sign of the core−shell motif with a more uniform surrounding of the water droplet by other species (see Figure 7h as compared to Figure 7g). Additional evidence of this core−shell motif was provided by the radial density profiles. Again in the analysis of these density distributions, the origin was placed at the COM of the water droplet. As evident from Figure 11c, the core region is exclusively occupied by the water molecules. Away from this inner core, 1-octanol oxygen is the first heavy atomic species to appear, followed by 1-octanol carbon and then *n*-nonane carbon. Given the amount of overlap in the density profiles, it is clear that water and *n*-nonane are barely in direct contact with each other but rather are connected through the intermediate surfactant layer of 1-octanol, thus ultimately confirming the onion-like core−shell structure formed by the larger clusters.

D. Implications of the Core−Shell Structure on Atmospheric Organic Aerosols and Beyond. The results obtained here are expected to have important implications for atmospheric organic nanodroplets. Being close models for those atmospheric systems, the core−shell structure and the related results/concepts (such as mutual nucleation enhancement) discovered here for water/*n*-nonane/1-alcohol are likely transferable to the aqueous organic aerosols formed in the atmosphere. In fact, such an "inverted micelle" structure has already been proposed to account for the high organic content found in many types of atmospheric aerosols, which would be otherwise inexplicable based on bulk solubilities.[31] This structure can be further linked to the cloud albedo enhancement through the surface tension reduction mechanism, an effect that would be largely missing in predictions yielded by the classical homogeneous, continuum model.[28] The small angle neutron scattering experiments[34] have recently provided some direct evidence of the formation of the core−shell structure for nanodroplets formed by water and 1-butanol, whereas this current work further suggests that the core−shell structure formed by longer alcohols (such as 1-octanol) or surfactants (which are more typical components for atmospheric aerosols) can lead to the formation of an additional organic layer to wrap around this structure. This interesting finding has added some new meaning to this "inverted micelle" picture. For example, this core−shell structure may serve as a natural condenser for collecting and concentrating those relatively nonpolar organic compounds. As a result, organic aerosols are a potential transport vehicle for these water insoluble compounds in the atmospheric environment.[31] Also the greatly enhanced local concentration of organic materials is expected to improve substantially the rate of chemical transformation for those species that are mutually

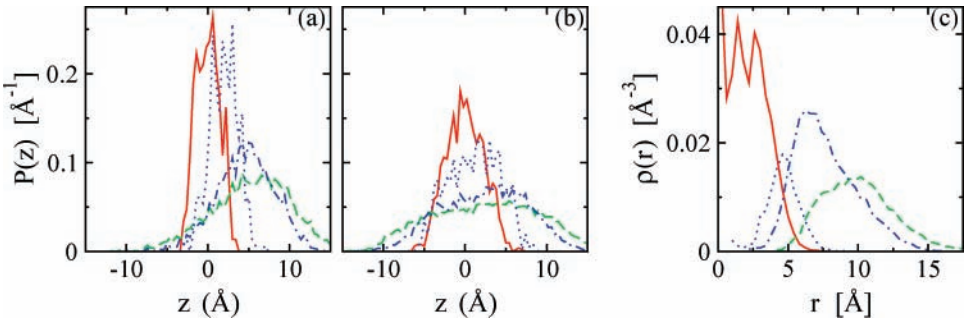

Figure 11. Probability density profiles along the *z*-axis (see text for the detailed definition) obtained for water oxygen (red solid), 1-octanol oxygen (blue dotted), 1-octanol carbon (blue dashed-dotted), and *n*-nonane carbon (green dashed). Panels a and b represent the results obtained for fully mixed clusters containing a total of 15 and 39 molecules, respectively. Shown in panel c are the radial density profiles obtained for the larger clusters of 39 molecules.

reactive with each other. On an entirely different topic, this core−shell structure coated by an additional "insulating" layer may be an ideal motif for encapsulation applications, e.g., to gain an optimal control of particle agglomeration and correspondingly particle size, important in the processing of nanomaterials.[55]

4. Conclusions

Using the AVUS-HR simulation approach, an extensive vapor−liquid nucleation study was carried out on the ternary water/*n*-nonane/1-alcohol ($C_iH_{2i+1}OH$) mixtures with $i = 2$, 4, 6, and 8. It was found from the onset activity results that all these systems exhibit the type of nonideal nucleation behavior that was previously discovered by experiments on the water/*n*-nonane/1-butanol mixture. However, there are subtle but important differences in the microscopic details with respect to the miscibility and structures formed by these three components. Specifically, for systems involving shorter alcohols (e.g., ethanol and 1-butanol), the most probable clusters found throughout the entire range of vapor-phase composition conditions are enriched by either water or *n*-nonane but not both. In contrast, for systems involving longer alcohols (1-hexanol and 1-octanol), we were able to locate appropriate conditions under which the nucleation pathways pass through critical nuclei that contain substantial amount of all three components. In fact, for water/*n*-nonane/1-octanol at an intermediate gas-phase activity composition, fully mixed clusters with a roughly equal molar amount of water, *n*-nonane, and 1-octanol appear as a major group of clusters on the nucleation landscape. Structural analysis revealed the microscopic origin for the enhanced miscibility observed between water and *n*-nonane—the formation of the core−shell (water−alcohol) structure. For example, this core−shell structure prepares a nonpolar surface that is more attractive for the adsorption of the purely nonpolar *n*-nonane than the original bare water surface. When 1-hexanol and 1-octanol are used, this core−shell structure induces a rather uniform dispersion of the *n*-nonane molecules at the outside that allows them to fully interact with the alkyl tail of the alcohol molecules. This compares favorably to the one-sided deposition of *n*-nonane found for clusters containing shorter alcohols, which remain as oil droplets fully segregated from the water molecules, consistent with the calculated miscibility data. This new finding of additional organic layers at the outside of the core−shell structure has important implications to other multicomponent nanodroplets, from encapsulation of nanomaterials to the transport of organic materials via atmospheric organic aerosols. Some of these results are testable experimentally given that the experimental measurements have been previously performed on mixtures containing water, *n*-nonane, and 1-butanol.

Acknowledgment. We thank Profs. Ilja Siepmann, James Donaldson, Gerald Wilemski, and Barbara Hale for many stimulating discussions and Prof. Les Butler and Heath Barnett for their kind help with the Amira software used for Figures 9 and 10. Financial support from the LSU start-up fund, the National Science Foundation (CHE/MCB-0448918), the Petroleum Research Fund, administered by the American Chemical Society (Grant No. 41933-G9), and Louisiana Board of Regents Support Fund (LEQSF(2005-08)-RD-A-02) is gratefully acknowledged. Part of the computer resources were provided by the Center for Computation and Technology, the Office of Computing Services at LSU, and the Louisiana Optical Network Initiative.

References and Notes

(1) Volmer, M.; Weber, A. *Z. Phys. Chem., Stöchiom. Verwandtschaftsl.* **1926**, *119*, 227.
(2) Becker, R.; Döring, W. *Ann. Phys. (Leipzig)* **1935**, *24*, 719.
(3) ten Wolde, P. R.; Frenkel, D. *J. Chem. Phys.* **1998**, *109*, 9919.
(4) ten Wolde, P. R.; Frenkel, D. *J. Chem. Phys.* **1998**, *109*, 9901.
(5) Oh, K. J.; Zeng, X. C. *J. Chem. Phys.* **2000**, *112*, 294.
(6) Yoo, S.; Oh, K. J.; Zeng, X. C. *J. Chem. Phys.* **2001**, *115*, 8518.
(7) Kusaka, I.; Wang, Z.-G.; Seinfeld, J. H. *J. Chem. Phys.* **1998**, *108*, 3416.
(8) Kusaka, I.; Oxtoby, D. W. *J. Chem. Phys.* **1999**, *110*, 5249.
(9) Kathmann, S. M.; Schenter, G. K.; Garrett, B. C. *J. Chem. Phys.* **1999**, *111*, 4688.
(10) Kathmann, S. M.; Schenter, G. K.; Garrett, B. C. *Phys. Rev. Lett.* **2005**, *94*, 116104.
(11) Merikanto, J.; Zapadinsky, E.; Vehkamäki, H. *J. Chem. Phys.* **2004**, *121*, 914.
(12) Lauri, A.; Merikanto, J.; Zapadinsky, E.; Vehkamäki, H. *Atmos. Res.* **2006**, *82*, 489.
(13) Chen, B.; Siepmann, J. I.; Oh, K. J.; Klein, M. L. *J. Chem. Phys.* **2001**, *115*, 10903.
(14) Chen, B.; Siepmann, J. I.; Oh, K. J.; Klein, M. L. *J. Chem. Phys.* **2002**, *116*, 4317.
(15) Chen, B.; Siepmann, J. I.; Klein, M. L. *J. Phys. Chem. A* **2005**, *109*, 1137.
(16) Nellas, R. B.; McKenzie, M. E.; Chen, B. *J. Phys. Chem. B* **2006**, *110*, 18619.
(17) Keasler, S. J.; Nellas, R. B.; Chen, B. *J. Chem. Phys.* **2006**, *125*, 144520.
(18) Chen, B.; Siepmann, J. I. *J. Phys. Chem. B* **2000**, *104*, 8725.
(19) Chen, B.; Siepmann, J. I. *J. Phys. Chem. B* **2001**, *105*, 11275.
(20) Torrie, G. M.; Valleau, J. P. *Chem. Phys. Lett.* **1974**, *28*, 578.
(21) Wilding, N. B. *Phys. Rev. E* **1995**, *52*, 602.
(22) Potoff, J. J.; Panagiotopoulos, A. Z. *J. Chem. Phys.* **1998**, *109*, 10914.
(23) Chen, B.; Siepmann, J. I.; Klein, M. L. *J. Am. Chem. Soc.* **2003**, *125*, 3113.
(24) McKenzie, M. E.; Chen, B. *J. Phys. Chem. B* **2006**, *110*, 3511.
(25) Nellas, R. B.; Chen, B.; Siepmann, J. I. *Phys. Chem. Chem. Phys.* **2007**, *9*, 2779.
(26) Nellas, R. B.; Chen, B. *Phys. Chem. Chem. Phys.* **2008**, *10*, 506.
(27) Viisanen, Y.; Strey, R. *J. Chem. Phys.* **1996**, *105*, 8293.
(28) Facchini, M. C.; Mircea, M.; Fuzzi, S.; Charlson, R. *J. Nature* **1999**, *401*, 257.

(29) Charlson, R. J.; Seinfeld, J. H.; Nenes, A.; Kulmala, M.; Laaksonen, A.; Facchini, M. C. *Science* **2001**, *292*, 2025.
(30) Li, J.-S.; Wilemski, G. *Phys. Chem. Chem. Phys*. **2006**, *8*, 1266.
(31) Ellison, G. B.; Tuck, A. F.; Vaida, V. J. *Geophys. Res*. **1999**, *104*, 11633.
(32) Dobson, C. M.; Ellison, G. B.; Tuck, A. F.; Vaida, V. *Proc. Natl. Acad. Sci. U.S.A*. **2000**, *97*, 11864.
(33) Donaldson, D. J.; Tuck, A. F.; Vaida, V. *Orig. Life Evol. Biosphere* **2002**, *32*, 237.
(34) Wyslouzil, B. E.; Wilemski, G.; Strey, R.; Heath, C. H.; Dieregsweiler, U. *Phys. Chem. Chem. Phys*. **2006**, *8*, 54.
(35) Tarek, M.; Klein, M. L. *J. Phys. Chem. A* **1997**, *101*, 8639.
(36) Siepmann, J. I.; Frenkel, D. *Mol. Phys*. **1992**, *75*, 59.
(37) Frenkel, D.; Mooij, G. C. A. M.; Smit, B. J. *Phys. Condens. Matter* **1992**, *4*, 3053.
(38) Martin, M. G.; Siepmann, J. I. *J. Phys. Chem. B* **1999**, *103*, 4508.
(39) Jorgensen, W. L.; Chandrasekhar, J.; Madura, J. D.; Impey, R. W.; Klein, M. L. *J. Chem. Phys*. **1983**, *79*, 926.
(40) Martin, M. G.; Siepmann, J. I. *J. Phys. Chem. B* **1998**, *102*, 2569.
(41) Chen, B.; Potoff, J. J.; Siepmann, J. I. *J. Phys. Chem. B* **2001**, *105*, 3093.
(42) Stillinger, F. H. *J. Chem. Phys*. **1963**, *38*, 1486.
(43) Viisanen, Y.; Wagner, P. E.; Strey, R. *J. Chem. Phys*. **1998**, *108*, 4257.
(44) Viisanen, Y.; Strey, R.; Laaksonen, A.; Kulmala, M. *J. Chem. Phys*. **1994**, *100*, 6062.
(45) Strey, R.; Viisanen, Y.; Wagner, P. E. *J. Chem. Phys*. **1995**, *103*, 4333.
(46) Oxtoby, D. W.; Kashchiev, D. *J. Chem. Phys*. **1994**, *100*, 7665.
(47) Ford, I. J. *J. Chem. Phys*. **1996**, *105*, 8324.
(48) Oxtoby, D. W.; Laaksonen, A. *J. Chem. Phys*. **1995**, *102*, 6846.
(49) Talanquer, V.; Oxtoby, D. W. *J. Chem. Phys*. **1996**, *104*, 1993.
(50) Talanquer, V.; Oxtoby, D. W. *J. Chem. Phys*. **1997**, *106*, 3673.
(51) Napari, I.; Laaksonen, A. *J. Chem. Phys*. **1999**, *111*, 5485.
(52) ten Wolde, P. R.; Frenkel, D. *J. Chem. Phys*. **1998**, *109*, 9919.
(53) Chen, B.; Siepmann, J. I.; Klein, M. L. *J. Am. Chem. Soc*. **2002**, *124*, 12232.
(54) Chen, B.; Siepmann, J. I. *J. Phys. Chem. B* **2006**, *110*, 3555.
(55) Shah, P. S.; Hanrath, T.; Johnston, K. P.; Korgel, B. A. *J. Phys. Chem. B* **2004**, *108*, 9574.